Chinese Physics Letters

LETTER

Asymmetric Focusing Metasurfaces with High-*Q* Factor and Strong Sidelobe Suppression

Cite as: Yunqiao Yin *et al.* 2026 *Chin. Phys. Lett.* **43** 080402

DOI CSTR

Recommended Articles

Acoustic Bilayer Gradient Metasurfaces for Perfect and Asymmetric Beam Splitting
Jiaqi Quan, Baoyin Sun, Yangyang Fu, Lei Gao, and Yadong Xu
Chin. Phys. Lett. **41**, (2024)

High-*Q* and Maximally Intrinsically Chiral Quasi-Bound States in the Continuum via Generative Adversarial Networks
Chen Zhong, Yi-Lin Wang, Jun-Wu Guo, E-Xian Liu, Jun Yi, Xin-Xing Zhou, and Jian-Jun Liu
Chin. Phys. Lett. **43**, 060401 (2026)

Acoustic Reconfigurable Metagratings with High Quality Factor for Anomalous Wavefront Control
Fu Xu, MengRu Jiang, Yu Chen, Junyi Yang, Zhanlei Hao, and Yadong Xu
Chin. Phys. Lett. **43**, 061002 (2026)

Global Cross-Attention Transformer for Zero-Shot Metasurface Inverse Design
Li Zhu, Yichen Wang, Guangming He, Ouling Wu, Hongsheng Chen, and Chao Qian
Chin. Phys. Lett. **43**, 040401 (2026)

Mid-Infrared Superchiral Field Induced by Quasi-Guided Mode in Diamond Metasurface
Hao Wang, Shu Chen, Xing Liu, Yanan Yu, Ziyi Lv, Shengxiang Shan, Tinghui Xiao, and Chongxin Shan
Chin. Phys. Lett. **42**, 120405 (2025)

Direct Generation of an Array with 78400 Optical Tweezers Using a Single Metasurface
Yuqing Wang *et al.*
Chin. Phys. Lett. **43**, 010606 (2026)

A series journal of Chinese Physical Society distributed by IOP Publishing

Chinese Physics Letters

Chin. Phys. Lett. **43** 080402 (2026)

LETTER

DOI: 10.1088/0256-307X/43/8/080402
CSTR: 32039.14.0256-307X.43.8.080402

Asymmetric Focusing Metasurfaces with High-Q Factor and Strong Sidelobe Suppression

Yunqiao Yin(殷允桥)[1], Ye Zhang(张烨)[1], Xiaofeng Xu(徐晓峰)[1], Jiaqi Quan(权家琪)[3,*], and Lei Gao(高雷)[1,2,4,*]

[1]School of Physical Science and Technology, & Collaborative Innovation Center of Suzhou Nano Science and Technology & Jiangsu Key Laboratory of Frontier Material Physics and Devices, Soochow University, Suzhou 215006, China
[2]Jiangsu Key Laboratory of Biophotonics & Suzhou Key Laboratory of Biophotonics & SZCU-ITU International Joint MetaCenter for Advanced Photonics and Electronics, Suzhou City University, Suzhou 215104, China
[3]School of Mathematics and Physics, Anhui Jianzhu University, Hefei 230601, China
[4]Jiangsu Physical Science Research Center, Nanjing 210093, China

*Corresponding authors. Email: austqjq@163.com; leigao@suda.edu.cn

Optical diodes equipped with asymmetric transmission properties are essential for logic gate design in advanced optical computing chips. However, a fundamental bottleneck in asymmetric systems is the need to balance multidimensional performance, such as simultaneously meeting the collaborative control requirements of quality factor and sidelobe influence, which limits their application in integrated photonics. To overcome this challenge, we develop a composite mechanism for achieving high-performance asymmetric focusing and design a bilayer metasurface by incorporating subtle periodic perturbations within the silicon nanobars. Numerical results demonstrate strong asymmetric focusing with a Q factor exceeding 8000, along with a focal point that exhibits perfect sidelobe immunity. Furthermore, the designed bilayer metasurface exhibits strong robustness, maintaining its performance despite disturbances. This work offers a novel pathway for designing asymmetric elements for precision on-chip applications.

Introduction

The unidirectional conductivity of diodes makes them an irreplaceable component in modern electronic circuits and devices [1,2]. Asymmetric transmission (AT) has attracted considerable research interest, and the concept has been rapidly extended to acoustic and elastic waves [3−9] and heat [10−12]. In optics, controlling the amplitude, polarization, and phase of transmitted light based on the incident direction is of great significance for various applications in optical science and engineering. However, traditional materials and theoretical methods for AT often suffer from issues such as large device size and low efficiency. Thanks to the novel optical properties and flexible controllability of metamaterials and metasurfaces [13,14], significant progress has been made in optical AT, making them an ideal platform for achieving AT. However, AT often requires a trade-off between efficiency and modulation depth. For example, thin dielectric metasurfaces cannot achieve arbitrary amplitude transformations with high efficiency, which limits the realization of arbitrary optical responses. In recent years, various novel physical effects brought about by Moiré superlattices in 2D materials, such as graphene, have aroused widespread interest. Inspired by this, researchers have recently devoted themselves to designing various bilayer artificial 2D materials, i.e., bilayer metasurfaces [15], and have discovered many novel wave phenomena, such as Moiré quasi-bound states [16] and magic-angle lasers [17]. Multilayer metasurfaces can relieve many constraints of single-layer metasurface. Bilayer metasurfaces have achieved many important applications through high-efficiency, arbitrary control over amplitude, phase, and polarization [18−20], such as chiral emission control [21], beam steering [22], linear [18,23] and nonlinear wavefront shaping [24], holography [25], spectral filtering [26], and aberration correction in metalenses [27]. Considerable efforts have been devoted to optical nonreciprocity and AT [28−31], ranging from nonreciprocal photonic devices to graphene-based and metasurface-based AT schemes. However, simultaneously achieving a high-Q factor, high efficiency, and sidelobe suppression within a single asymmetric focusing device remains unexplored.

Recently, researchers have utilized interlayer coupling regulation mechanisms to design bilayer metasurfaces to achieve focusing with strong sidelobe suppression at subwavelength scales [32]. Such metalenses are expected to demonstrate great potential in fields such as quantum communication, optical micromanipulation, and optical micro-nanoprocessing. Unfortunately, these metalenses exhibit poor quality factor (Q factor) performance. In fact, the Q factor is crucial for the performance of many novel optical phenomena and other practical applications, such as filters [33], sensing [34], lasing [35], nonlinear optics [36], laser stealth [37], and photodetection [38]. Besides that, guided-mode resonance (GMR) can be achieved by combining a waveguide with a shallow grating. The high coherence of the nonlocal guided modes in the waveguide contributes to the observation of a high-Q factor in GMRs. In recent years, metasurfaces based on GMR have been proposed for investigating amplitude and phase modulators [39,40], third-harmonic generation [41], quantum-optical sources [42,43], splitters [44], and beam steerers [45,46]. Therefore, it has been proposed to generate high-Q metasurface lenses by introducing subtle structural perturbations into individual metasurface elements [47]. So far, despite advances in low-sidelobe bilayer metalenses [32], high-Q perturbed metasurfaces [47], and experimentally realized GMRs in notched silicon waveguides [41], there remains no viable strategy to simultaneously address all three aspects: efficiency, Q factor, and multidimensional wavefront manipulation, in multilayer metasurface-based wavefront shaping.

In this work, we propose bilayer metasurfaces that simultaneously realize optical AT and high-Q focusing, while achieving strong sidelobe suppression at the subwavelength scale. By introducing structural notches into the silicon nanostructures, we excite GMR, resulting in a significantly higher-Q factor. The introduction of periodic perturbations, which compensate for the momentum mismatch between the GMR inside the waveguide and free-space radiation, plays a pivotal role in achieving high transmission efficiency. Furthermore, considering the large sidelobes of traditional optical asymmetric

Received 11 March 2026; accepted 20 July 2026; published 19 August 2026
© 2026 Chinese Physical Society and IOP Publishing Ltd. All rights, including for text and data mining, AI training, and similar technologies, are reserved.

Check for updates

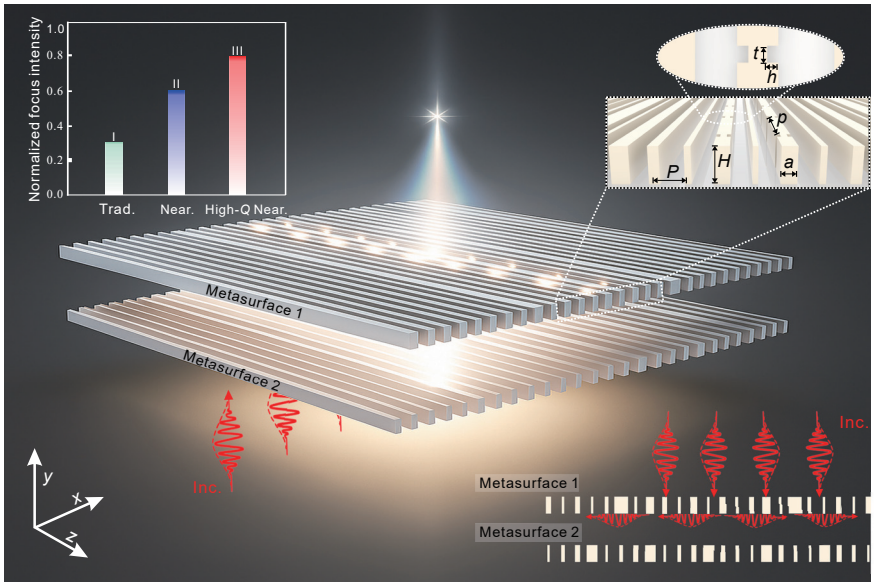

Fig. 1. Conceptual diagram of the asymmetric focusing metalens. Incident waves are launched from either the top or bottom side of the metalens. In the high-transmission and focusing case, the incident wave impinges on metasurface 2; in the low-transmission case, it impinges on metasurface 1. The upper-left inset shows the normalized focal intensity comparison among three types of asymmetric metalenses. The upper-right inset presents a zoomed-in view of the region highlighted by the dashed white line in metasurface 1, revealing the grating structure and the geometry of a representative subset of the high-Q structure.

focusing designs, the design theory of the asymmetric focusing lens (AFL) is further optimized to achieve asymmetric focusing with strong sidelobe suppression at the subwavelength scale. Next, we demonstrate that this design readily achieves Q values exceeding 1000 and near-field intensity enhancements over 10000. Importantly, we verify that the response of the bilayer device exhibits strong robustness to the horizontal and vertical alignment between the two layers, rendering its fabrication feasible with current technology. Overall, we envision that the AFL, owing to its advantages in strong sidelobe suppression and high-Q factors, holds significant potential for advanced applications in optical micromanipulation, sensing, imaging, and quantum communication.

Figure 1 schematically illustrates the multifunctional double-layer metalens, a metasurface-based device specifically designed for asymmetric energy transmission and manipulation. The primary objective of this article is to demonstrate the feasibility of achieving asymmetric focusing using double-layer metasurfaces that integrate multiple fundamental functionalities. A metalens must satisfy two key requirements: effectively collecting and capturing signals from the desired direction within the operational region, and efficiently blocking interference signals originating from the opposite direction. By carefully engineering the phase profile of the metasurfaces, we ensure that the forward-propagating beam is focused to a single point, whereas the backward-propagating beam is effectively blocked. For incident waves from the bottom side, the transmitted wave passes through metasurface 2 (MS2) followed by metasurface 1 (MS1) and is focused onto a single point above the lens. In contrast, for incident waves from the top side, the wave transmitted through MS1 undergoes a 90° rotation, propagates along the surface of MS1, and rapidly decays away from the interface, resulting in negligible optical energy transmission through MS2. Here, each individual nanobar in the metasurface acts as a phase "pixel," with its geometric dimensions determining the phase shift. The upper-right insets illustrate the detailed geometry of the grating, which consists of m unit cells with a spacing of P; each unit cell is composed of amorphous silicon nanobars of height H and width a.

The upper-left inset of Fig. 1 depicts the differences in focusing intensity among three types of metalenses, ranging from a conventional design to an optimized sidelobe-suppressed configuration. When illuminated by a plane wave, conventional metalenses can focus light onto the focal point, but the resulting focal spot is accompanied by significant sidelobes. This limitation arises from low transmissive focusing intensity, attributed to the drawbacks of the central region of the upper metasurface (MS1), which remains optically inactive during focusing. By optimizing the design theory of AFL, we achieve focusing with strong sidelobe suppression at the subwavelength scale, enabling the central region of MS1 to actively participate in the focusing process. Furthermore, we introduce periodic rectangular notches along the edges of the nanobars in the z-direction, with period p, width t, and depth h. As shown in the upper-right inset, these periodic notches are incorporated into a group of nanobars located near the center of MS1. Notably, this periodic perturbation compensates for the momentum mismatch between the guided resonant modes inside the waveguide and free-space radiation, thereby enabling excitation of GMR. Crucially, GMR is excited only over a narrow wavelength range, producing intense resonant fields and consequently yielding a high-Q factor. Therefore, it is imperative to design asymmetric metalenses capable of sidelobe suppression while simultaneously delivering high-Q factor and high efficiency, features that will significantly enhance the quality of focusing and imaging.

We report a silicon nanostructure designed to satisfy the phase distribution requirements of MS1 and MS2. Figure 2(a) schematically illustrates the cross-section of an individual supercell in the xz plane. Full-wave numerical simulations were performed using the commercial simulator COMSOL Multiphysics. The height of the nanobar is set to $H = 700$ nm, and the period is designed as $P = 600$ nm. The width a is treated as a tunable parameter to achieve a phase shift spanning the full range from 0 to 2π. Floquet boundaries were used on either side of nanobar and port boundaries, polarized into the plane, were used above and below the nanobars. Figure 2(b) shows the transmission (red curve) and phase delay (black curve) of the unit cell as a function of the tunable width a. In the simulations, the silicon nanobars were modeled as lossless materials, since absorption losses in silicon are negligible in the near-infrared region. Figure 2(c) shows the phase distributions (φ_1 and φ_2) of MS1 and MS2, respectively, where the black lines represent the theoretical phase distributions, and the red points denote the discrete phases of the 25 designed nanobars of MS1 and MS2 in the AFL.

It is well known that high refractive index materials support optical modes across a continuous spectrum. The momentum of these modes lies outside the range accessible by free-space light. Consequently, these modes cannot be accessed using normally incident free-space light, and thus do not exhibit resonant behavior in the far field. These modes are confined to this region and decay exponentially into

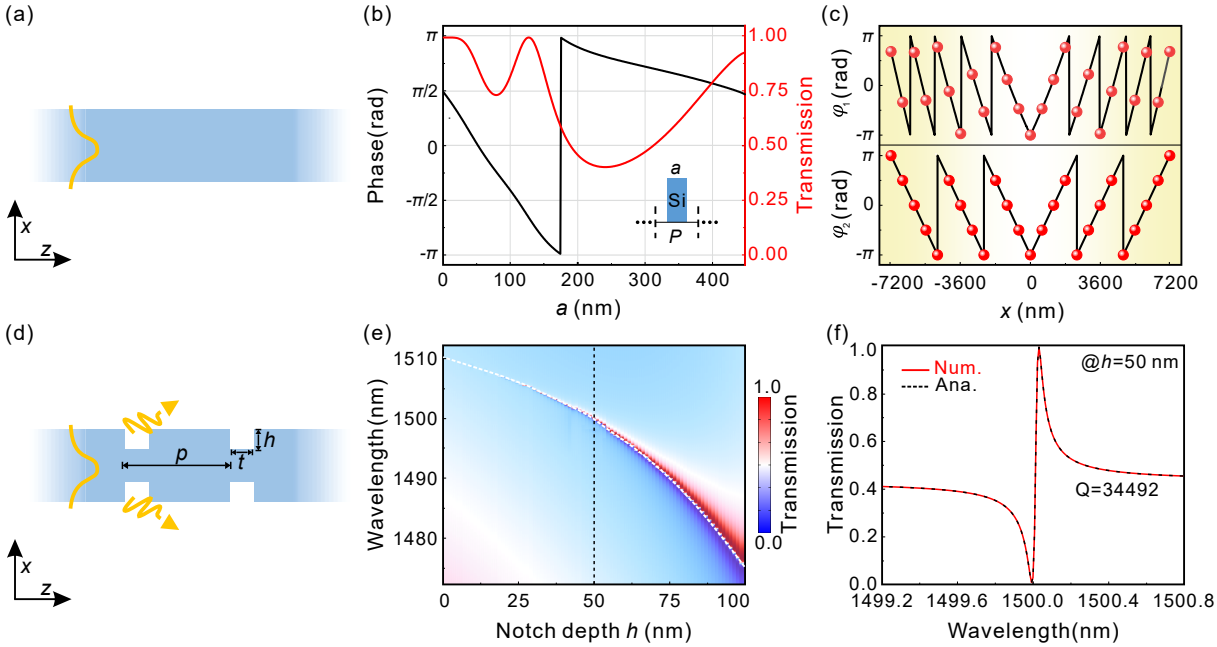

Fig. 2. (a) Schematic diagram of nanobars without notches. (b) Phase (black solid line) and transmission (red dashed line) as a function of width a. (c) The phase distributions of MS1 and MS2, respectively, in which the black lines are the theoretical phase distributions, and the red points represent the discrete phases of the 25 designed nanobars of MS1 and MS2 in the asymmetric focusing metalens. (d) Schematic of nanobars with notches (width t and depth h) along the length of the slab according to period p. (e) The transmission spectra as functions of notch depth h. (f) Transmission spectrum at $h = 50$ nm.

the vacuum. Moreover, due to the relationship between spatial periodicity and crystal momentum in periodic structures (similar to the relationship between time and frequency), specific periodic perturbations can be introduced into an infinite system to impart additional momentum at certain wavelengths. As shown in Fig. 2(d), we introduce periodic rectangular notches along the edges of the nanobars in the z-direction. As the notch period folds the below-light-line guided mode into the light cone, the resulting GMR constitutes a quasi-bound states in the continuum whose radiative Q is set by the perturbation depth h. Through this method, we can excite narrowband modes that are observable in the far field at selected wavelengths.

The transmission spectra are shown in Fig. 2(e) as functions of the notch depth h. We observe that a resonator with an infinite Q factor at $h = 0$ nm transforms into a high-Q resonator whose radiation loss grows with h. With fine-tuning, the broad transmission spectra remain largely unaffected by such minor perturbations. Figure 2(f) shows the detailed transmission spectrum (red solid line). By analyzing the transmission spectra of the structure, we can use the classical Fano formula to describe the observed peak positions and linewidths, which correspond to the real and imaginary parts of the eigenmode frequencies. Therefore, the transmission T is strictly described by the Fano formula. The fitting formula is as follows:

$$T(\omega) = \left| a_{\mathrm{r}} + \mathrm{i}a_{\mathrm{i}} + \frac{b}{\omega - \omega_0 + \mathrm{i}\gamma} \right|^2, \tag{1}$$

where a_{r} is the real background coefficient, a_{i} is the imaginary background coefficient, ω_0 is the oscillation frequency, γ is the damping coefficient of the metasurfaces, and b is a constant. Based on the analysis results, we can calculate the radiative quality factor $Q_{\mathrm{rad}} = \omega_0/(2\gamma)$. Additionally, the more subtle the perturbation required to approach the ideal bound mode with a theoretical Q approaching infinity, the greater the potential Q factor. Fabrication-induced scattering (sidewall roughness, dimensional disorder) contributes an extrinsic Q_{loss} ($1/Q_{\mathrm{total}} = 1/Q_{\mathrm{rad}} + 1/Q_{\mathrm{loss}}$). Since Q_{rad} is tunable via h, radiation loss can be made dominant, preserving the high-Q performance.

Asymmetric transmission has attracted considerable attention due to its potential value in integrated optics, and our high-Q approach can be applied to realize many other known metasurface designs. Let us first consider a conventionally designed double-layer asymmetric metalens [the design process can be found in the Supplementary Materials (SM)]. Figures 3(a) and 3(d) show the numerical results of the designed metalens under illumination from different incident directions, respectively. The fields exhibit the obvious asymmetric focusing phenomenon. The corresponding field distributions of incident and transmitted waves are displayed in the left and right panels of Figs. 3(a) and 3(d). For incidence from the right side, the transmitted wave is enhanced at the surface of MS1 and decays exponentially away from the interface, thereby preventing the light wave from passing through MS2. In this case, the transmitted wave exists as the surface mode on MS1 (see the SM for a detailed derivation). Furthermore, to more clearly reveal the asymmetric focusing effect, we have plotted the normalized intensity along the dashed line $\mathrm{L_I}$ [Fig. 3(a)] and the dashed line $\mathrm{R_I}$ [Fig. 3(d)] in Fig. 3(g). It can be clearly seen that the AFL simultaneously achieves AT and focusing, enabling its use in more complex optical fields. However, its sidelobe is too large, which is not conducive to practical application.

Next, we analyzed the cause of the large sidelobes in the asymmetric focusing shown in Fig. 3(a) and optimized the AFL structure to achieve asymmetric focusing with strong sidelobe suppression. According to the analysis based on Eqs. (S3) and (S4) in the SM, more than one-third of the central region of MS1 does not participate in focusing. Consequently, fewer optical wave components contribute to the focal spot, leading to significant sidelobes. To suppress these sidelobes and achieve improved focusing, the central region of MS1 must be utilized as effectively as possible for focusing. Therefore, the direction of the refraction angle induced by MS2 should be opposite to that shown in Fig. S2 of the SM, allowing the light waves to pass through the central region of MS1. The theoretical model of the focusing and transmission path is illustrated in Fig. S3 of the SM. Meanwhile, to ensure that light waves incident from the right side are converted by MS1 into surface waves, the relationship between the transmission angles θ_{i2m} and α_{t2m} must satisfy: $\sin\alpha_{t2m} - \sin\theta_{i2m} > \sin\alpha_{t2(m+1)} - \sin\theta_{i2(m+1)} \geqslant 1$. Based on the above analysis, we can obtain the optimized phase profiles of the double-layer metasurfaces for the AFL and the corresponding field distribution exhibiting near-zero-sidelobe asymmetric focusing, as shown in Figs. 3(b) and 3(e). Additionally, to more clearly reveal the asymmetric focusing effect after optimization,

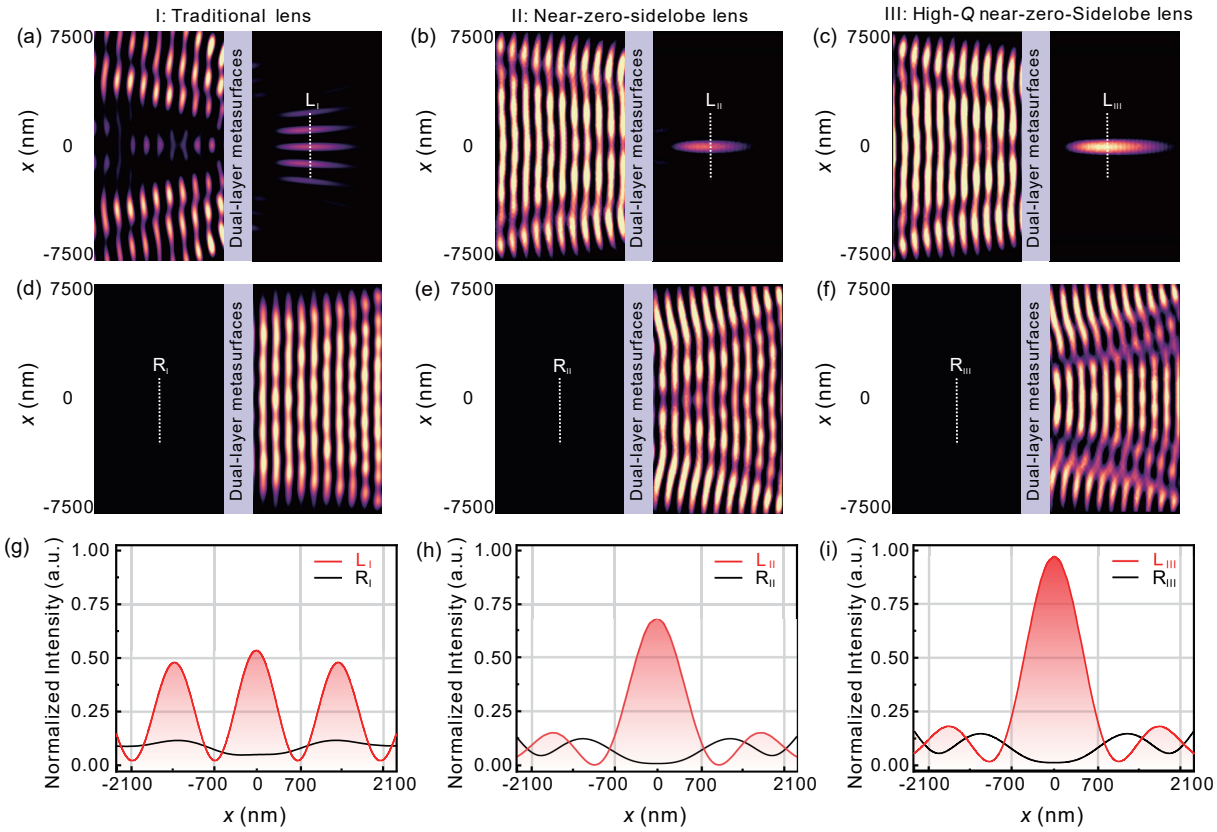

Fig. 3. (a)–(c) Forward incidence: comparison of the spatial distribution of field strength for three types of lenses. (d)–(f) Backward incidence: comparison of the spatial distribution of field strength for three types of lenses. The normally incident waves are represented by black arrows. (g) The normalized intensity along the dashed line L_I and the dashed line R_I. (h) The normalized intensity along the dashed line L_{II} and the dashed line R_{II}. (i) The normalized intensity along the dashed line L_{III} and the dashed line R_{III}.

we have plotted the normalized intensity along the dashed line L_{II} [Fig. 3(b)] and the dashed line R_{II} [Fig. 3(e)] in Fig. 3(h). As clearly seen from the line profiles in Fig. 3(h), the sidelobes are significantly smaller than those in Fig. 3(g), indicating that the sidelobes in asymmetric focusing can be effectively suppressed.

For the high-Q metalens design, both MS1 and MS2 consist of 25 discrete nanobars each, and the lens is designed to have a focal length of 8 μm at a wavelength of 1500 nm. Periodic notches are etched in the set of nanobars (with width $a = 295$ nm) adjacent to the metalens center in MS1. This notch design induces a GMR near the 1500 nm wavelength. The corresponding field distributions are displayed in Figs. 3(c) and 3(f) for comparison with the metalens in which GMR is not excited. We also plotted the normalized intensity along the dashed line L_{III} [Fig. 3(c)] and the dashed line R_{III} [Fig. 3(f)] in Fig. 3(i). Asymmetric response of the transmitted waves may be seen for angularly opposite incidences. Figures 3(h) and 3(i) confirm the focusing capabilities of the low-Q and high-Q metalenses at an incident wavelength of 1500 nm. The full width at half maximum is 910 nm for the low-Q metalens and 877 nm for the high-Q metalens. Note that the higher focal intensity of the high-Q lens is not necessarily a direct result of the high-Q resonance itself. Nevertheless, our metalens design still achieves powerful focusing performance. Overall, we conclude that by optimizing the design of traditional AFLs, effective suppression of large sidelobes caused by insufficient light wave participation can be achieved. Furthermore, by introducing the GMR mechanism, narrowband resonant enhancement with a high Q is achieved at specific wavelengths, significantly enhancing its applicability in high-sensitivity sensing and narrow-linewidth optical manipulation.

Figure 4(a) shows the normalized intensity of metalenses with and without notches, exhibiting a distinct Fano resonance feature. Note that the spectrum is obtained by integrating the field intensity over the focal plane (xy-plane) located at the designed focal distance of 8 μm from the metalens and normalized to the average intensity of the incident unmodified Gaussian beam. As shown, the notched metasurface exhibits a high-Q resonance at a wavelength of $\lambda = 1500.2$ nm, associated with a Q factor of approximately 8600. As illustrated in the inset of Fig. 4(a), the near-field distribution around the nanobars reveals a maximum field enhancement of approximately 1.42×10^4 for the notched case, significantly higher than that of the unnotched case. Note that the narrow operating bandwidth is a fundamental consequence of the time–bandwidth product; the high-Q factor is achieved by trading bandwidth for resonant enhancement, with Q continuously tunable via the notch depth h. To quantitatively characterize the performance of AT, we define the asymmetry factor of transmitted energy as $\eta = |T_{\text{positive}} - T_{\text{negative}}|/(T_{\text{positive}} + T_{\text{negative}})$, where T_{negative} and T_{positive} denote the transmittance for waves incident along the $-y$ and $+y$ directions, respectively. In both incidence cases, the transmitted energy is measured at a distance of 8 μm from the metalens. Figure 4(b) shows the relationship between the energy transmission asymmetry factor η and the incident wavelength. The red curve and black curve correspond to the notched and unnotched metalens, respectively.

Moreover, when designing double-layer metasurface devices, it is highly important to evaluate the tolerance of the optical response to both lateral (horizontal) and vertical interlayer misalignments. Firstly, we have assumed that the distance between the two layers is fixed and have verified that the response of the double-layer device is unaffected by horizontal displacements between the two metasurface layers. We introduce a shift ∇x [see the sketch in Fig. 5(a)], which quantifies the horizontal displacement of MS1 relative to its position considered in previous cases. Figure 5(b) shows the results of the focused optical fields of the double-layer device for various values of ∇x (from $\nabla x = -200$ nm to $\nabla x = 200$ nm). Furthermore, to more clearly illustrate the impact of horizontal shift on the focusing effect, we have plotted the normalized intensity at the corresponding focal spots in Fig. 5(c). These calculations confirm that the focusing strength of the double-layer device has a weak dependence on ∇x. Notably, as $|\nabla x|$

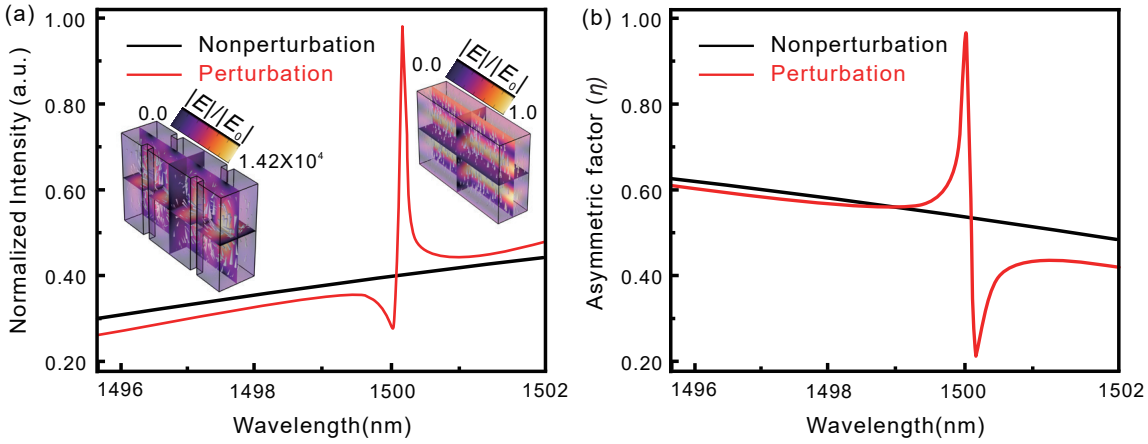

Fig. 4. (a) The normalized intensity spectral response of the notched (red line) and unnotched lenses (black line). The insets show near-field calculations of the nanobars for the notched and unnotched lenses. (b) The relationship between the energy transmission asymmetry factor and the incident wavelength.

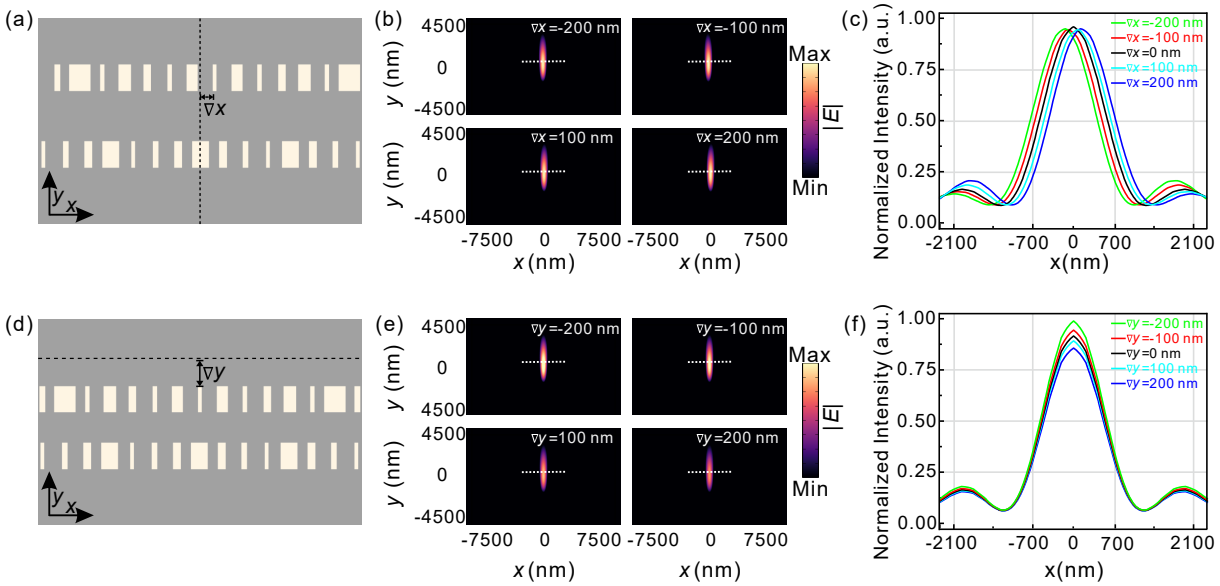

Fig. 5. Impact of vertical and horizontal misalignments on the response of the bilayer device. (a) Schematic diagram of introducing a horizontal shift ∇x. (b) The focused optical fields of the bilayer metasurfaces for various values of ∇x. (c) The normalized intensity at the corresponding focal spots in (b). (d) Schematic diagram of introducing a vertical shift ∇y. (e) The focused optical fields of the bilayer metasurfaces for various values of ∇y. (f) The normalized intensity at the corresponding focal spots in (e).

increases, there is a slight shift in the focal spot. Notably, GMRs in notched silicon waveguides have been experimentally realized [41]; combined with the demonstrated misalignment tolerance, this indicates that the proposed design is experimentally feasible with current silicon nanofabrication technology. As these calculations clearly demonstrate, the response of the double-layer device is entirely independent of the horizontal displacement between the two metasurfaces.

Next, we assume that the two layers are aligned horizontally so that their unit cells share the same symmetry plane [Fig. 5(d)]. In Figs. 5(e) and 5(f) , we investigate how the response of the double-layer device depends on the vertical shift ∇y. Figure 5(e) shows the results of the focused optical field of the double-layer device for different values of ∇y (from $\nabla y = -200$ nm to $\nabla y = 200$ nm). Moreover, to more clearly reveal the effect of the vertical offset on the focusing effect, we plot the normalized intensity at the corresponding focal point in Fig. 5(f). Particularly, although there is no change in the position of the focal point, its intensity gradually increases as ∇y decreases. We attribute this result to near-field interactions between the layers. Importantly, the results in Fig. 5 confirm that our device is highly robust against large horizontal or vertical misalignments between MS1 and MS2, which is a crucial feature for its practical fabrication and implementation in realistic scenarios.

In summary, we propose strongly asymmetric focusing metasurfaces with high-Q factor and sidelobe immunity and demonstrate their utility in the AT regime. By elaborately engineering the geometric size of the silicon nanobar notches, we combine diffractive metasurfaces with high-Q GMR to achieve efficient AT. With this bilayer metasurface, we compare the changes in the focal spot of three types of asymmetric metalenses. The design exhibits strong asymmetry at the operating wavelength. In addition, we have demonstrated that the response of the bilayer device is essentially independent of the interlayer spacing and horizontal displacement, which is crucial for the practical manufacturing of these devices. In the future, we envision significant potential for enhancing the performance of multilayer metasurfaces by integrating them with various high-Q metasurface techniques and nonreciprocal optical systems.

Acknowledgements

This work was supported by the National Natural Science Foundation of China (Grant Nos. 12274314 and 12474313), the Suzhou Basic Research Project (Grant No. SJC2023003).

References

[1] Fan J, Han C, Yang G, Song B, Xu R, Xiang C, Zhang T, and Qian L 2024 *Adv. Mater.* **36** 2312948
[2] Furlan F, Moreno-Naranjo J M, Gasparini N, Feldmann S, Wade J, and Fuchter M J 2024 *Nat. Photon.* **18** 658
[3] Xia J, Zhang X, Sun H, Yuan S, Qian J, and Ge Y 2018 *Phys. Rev. Appl.* **10** 014016
[4] Nassar H, Yousefzadeh B, Fleury R, Ruzzene M, Alù A, Daraio C, Norris A N, Huang G, and Haberman M R 2020 *Nat. Rev. Mater.* **5** 667
[5] He J, Zhang S, Zheng P, Fang X, Sui D, Yao H, Ke X, Ling D, Sun M, Huang K, and Ou X 2025 *Nat. Commun.* **16** 11587
[6] Fu P, Yang T, and Chen L 2025 *Adv. Funct. Mater.* **35** 2419986
[7] Chen Z, Li Z, Weng J, Liang B, Lu Y, Cheng J, and Alù A 2023 *Sci. Bull.* **68** 2164
[8] Quan J, Sun B, Fu Y, Gao L, and Xu Y 2024 *Chin. Phys. Lett.* **41** 014301
[9] Hu J, Liang B, and Qiu X J 2018 *Chin. Phys. Lett.* **35** 024301
[10] Yang J, Liu M, Wang T, Meng G, Wang Z, Guo C, Lin K, Lin H, and Jia B 2024 *Small* **20** 2402575
[11] Xu Z, Liu C, Wang X, Li Y, and Bai Y 2024 *Int. J. Miner Metall Mater* **31** 1678
[12] Shrestha R, Luan Y, Luo X, Shin S, Zhang T, Smith P, Gong W, Bockstaller M, Luo T, Chen R, Hippalgaonkar K, and Shen S 2020 *Nat. Commun.* **11** 4346
[13] Li Z, Zhou L, Liu Z, Panmai M, Li S, Liu J, and Lan S 2023 *ACS Photonics* **10** 206
[14] Chen Y, Fleury R, Seppecher P, Hu G, and Wegener M 2025 *Nat. Rev. Phys.* **7** 299
[15] Arbabi A, Arbabi E, Horie Y, Kamali S M, and Faraon A 2017 *Nature Photon.* **11** 415
[16] Huang L, Zhang W, and Zhang X 2022 *Phys. Rev. Lett.* **128** 253901
[17] Mao X R, Shao Z K, Luan H Y, Wang S L, and Ma R M 2021 *Nat. Nanotechnol.* **16** 1099
[18] Zheng H, He M, Zhou Y, Kravchenko I I, Caldwell J D, and Valentine J G 2022 *ACS Nano* **16** 15100
[19] Overvig A C, Shrestha S, Malek S C, Lu M, Stein A, Zheng C, and Yu N 2019 *Light Sci. Appl.* **8** 92
[20] Mirzapourbeinekalaye B, McClung A, and Arbabi A 2022 *Adv. Opt. Mater.* **10** 2102591
[21] Gromyko D, An S, Gorelik S, Xu J, Lim L J, Lee H Y L, Tjiptoharsono F, Tan Z K, Qiu C W, Dong Z, and Wu L 2024 *Nat. Commun.* **15** 9804
[22] Zhang L, Zhang L, Xie R, Ni Y, Wu X, Yang Y, Xing F, Zhao X, and You Z 2023 *Adv. Sci.* **10** 2300542
[23] Dorrah A H, Park J S, Palmieri A, and Capasso F 2025 *Nat. Commun.* **16** 3126
[24] Qu L, Wu W, Zhang D, Wang C, Bai L, Li C, Cai W, Ren M, Alù A, and Xu J 2025 *Nano Lett.* **25** 4854
[25] Georgi P, Wei Q, Sain B, Schlickriede C, Wang Y, Huang L, and Zentgraf T 2021 *Sci. Adv.* **7** eabf9718
[26] Lee C, Jeon S, Kim S J, and Kim S J 2023 *Opt. Express* **31** 4920
[27] Li X, Cai X, Liu C, Kim Y, Badloe T, Liu H, Rho J, and Xiao S 2024 *OEA* **7** 240085
[28] Ferreira A, Viana-Gomes J, Bludov Yu V, Pereira V, Peres N M R, and Castro Neto A H 2011 *Phys. Rev. B* **84** 235410
[29] Zhou Y, Dong Y Q, Fan R H, Hu Q, Peng R W, and Wang M 2014 *Appl. Phys. Lett.* **105** 041114
[30] Sounas D L and Alù A 2017 *Nat. Photon* **11** 774
[31] Zhu Y, Hou Y H, Cai Q, Chen L J, Peng R W, and Wang M 2026 *Nano Lett.* **26** 5504
[32] Xie J, Liang S, Liu J, Tang P, and Wen S 2020 *Annalen der Physik* **532** 2000035
[33] Williams C, Gordon G S D, Wilkinson T D, and Bohndiek S E 2019 *ACS Photonics* **6** 3132
[34] Tittl A, Leitis A, Liu M, Yesilkoy F, Choi D Y, Neshev D N, Kivshar Y S, and Altug H 2018 *Science* **360** 1105
[35] Huang C, Zhang C, Xiao S, Wang Y, Fan Y, Liu Y, Zhang N, Qu G, Ji H, Han J, Ge L, Kivshar Y, and Song Q 2020 *Science* **367** 1018
[36] Santiago-Cruz T, Gennaro S D, Mitrofanov O, Addamane S, Reno J, Brener I, and Chekhova M V 2022 *Science* **377** 991
[37] Pan M, Huang Y, Li Q, Luo H, Zhu H, Kaur S, and Qiu M 2020 *Nano Energy* **69** 104449
[38] Hong J, Van De Groep J, Lee N, Kim S J, Lalanne P, Kik P G, and Brongersma M L 2023 *Optica* **10** 134
[39] Kwon H, Zheng T, and Faraon A 2021 *Nano Lett.* **21** 2817
[40] Forouzmand A and Mosallaei H 2019 *ACS Photonics* **6** 2860
[41] Wang Z, Zhao Q, Tang W, Gao Y, He J, Zhu Y, Wang S, Yu H, Peng R, and Wang M 2024 *Appl. Phys. Lett.* **124** 101101
[42] Yin Y, Zhang Y, Xu X, and Gao L 2025 *Opt. Express* **33** 23883
[43] Zhou N, Zheng S, Cao X, Zhao Y, Gao S, Zhu Y, He M, Cai X, and Wang J 2019 *Sci. Adv.* **5** eaau9593
[44] Klopfer E, Dagli S, Iii D B, Lawrence M, and Dionne J A 2022 *Nano Lett.* **22** 1703
[45] Lawrence M, Barton D R, and Dionne J A 2018 *Nano Lett.* **18** 1104
[46] Lawrence M, Barton D R, Dixon J, Song J H, Van De Groep J, Brongersma M L, and Dionne J A 2020 *Nat. Nanotechnol.* **15** 956
[47] Klopfer E, Lawrence M, Barton D R, Dixon J, and Dionne J A 2020 *Nano Lett.* **20** 5127